Potential of C-band Synthetic Aperture Radar Sentinel-1 time-series for the monitoring of phenological cycles in a deciduous forest

Kamel Soudani, Nicolas Delpierre, Daniel Berveiller, Gabriel Hmimina, Gaëlle Vincent, Alexandre Morfin, Éric Dufrêne

Contents lists available at ScienceDirect

International Journal of Applied Earth Observations and Geoinformation

journal homepage: www.elsevier.com/locate/jag
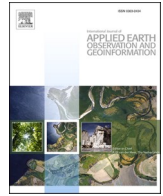
Potential of C-band Synthetic Aperture Radar Sentinel-1 time-series for the monitoring of phenological cycles in a deciduous forest

Kamel Soudani [a,*], Nicolas Delpierre [a,b], Daniel Berveiller [a], Gabriel Hmimina [c], Gaëlle Vincent [a], Alexandre Morfin [a], Éric Dufrêne [a]

[a] *Université Paris-Saclay, CNRS, AgroParisTech, Ecologie Systématique et Evolution, 91405 Orsay, France*
[b] *Institut Universitaire de France (IUF), France*
[c] *Laboratoire de Météorologie Dynamique, IPSL, CNRS/UPMC, Paris, France*

ARTICLE INFO

ABSTRACT

Annual time-series of the two satellites C-band SAR (Synthetic Aperture Radar) Sentinel-1A and 1B data over five years were used to characterize the phenological cycle of a temperate deciduous forest. Six phenological metrics of the start (SOS), middle (MOS) and end (EOS) of budburst and leaf expansion stage in spring, and the start (SOF), middle (MOF) and end (EOF) of leaf senescence in autumn were extracted using an asymmetric double sigmoid function (ADS) fitted to the time-series of the ratio (VV/VH) of backscattering at co-polarization VV (vertical–vertical) and at cross polarization VH (vertical-horizontal). Phenological metrics were also derived from other four vegetation proxies (Normalized Difference Vegetation Index NDVI time-series from Sentinel-2A and 2B images, and in situ measurements of NDVI measurements, Leaf Area Index LAI and litterfall temporal dynamics). These estimated phenological metrics were compared to phenological observations obtained by visual observations from the ground, achieved using binoculars by three inter-calibrated observers, on a bi-weekly basis during the budburst and weekly during the senescence. We observe a decrease in the backscattering coefficient (σ^0) at VH cross polarization during the leaf development and the expansion phase in spring and an increase during the senescence phase, contrary to what is usually observed on various types of crops. In vertical polarization, σ^0VV shows very little variation throughout the year. S-1 time-series of VV/VH ratio provide a good description of the seasonal vegetation cycle allowing the estimation of spring and autumn phenological metrics. Estimates provided by VV/VH of budburst dates using MOS criterion differ by approximately 8 days on average (mean average deviation) from phenological observations. During senescence phase, estimates using MOF criterion are later and deviate by about 20 days from phenological observations of leaf senescence while the differences are of the order of 2 to 4 days between the phenological observations and estimates based on in situ NDVI and LAI time-series, respectively. A deviation of about 7 days, comparable to that observed during budburst, is obtained between the estimates of senescence (MOF) from S-1 and those determined from the in situ monitoring of litterfall. While in spring, leaf emergence and expansion described by LAI or NDVI explain the increase of VV/VH (or the decrease of σ^0VH), during senescence, S-1 VV/VH is decorrelated from LAI or NDVI and is better explained by litterfall temporal dynamics. This behavior resulted in a hysteresis phenomenon observed on the relationships between VV/VH and NDVI or LAI. For the same LAI or NDVI, the response of VV/VH is different depending on the phenological phase considered. This study shows the high potential offered by Sentinel-1 SAR C-band time-series for the detection of forest phenology, thus overcoming the limitations caused by cloud cover in optical remote sensing of vegetation phenology.

1. Introduction

In forest ecosystems, the opening of buds ("budburst") in spring and the coloration and fall of leaves ("leaf senescence") mark the start and the end of the photosynthetically active period and therefore play a key role in their productivity and carbon storage activity (Richardson et al., 2010). Historically, the timings of these phenological events have been monitored through direct and periodic human observations of trees in

the field. However, this method is time-consuming, laborious, non-standardized and subject to an observer effect (Schaber and Badeck, 2002). Alternative indirect field techniques (RGB camera, proximal remote sensing systems, micrometeorological radiation sensors, etc.) are also used to monitor the seasonal cycle of forest canopy (Soudani et al., 2021). However, phenological metrics derived from both direct field observations and indirect proximal techniques are spatially sparse and fail to describe the spatial variability in phenology due to the vegetation diversity (Soudani et al., 2012). Satellite based remote sensing, because of its great potential for spatial sampling, constitutes the main approach for estimating and mapping phenological metrics at local to regional scales (Reed et al., 2003). However, the assessment of this potential has been severely limited by the difficulty of linking satellite-derived phenological metrics to field phenological observations, mainly due to temporal and spatial scale mismatches (Fisher et al., 2006). A few years ago, constellations of identical satellites such as SPOT 6/7, Pleiades, and more particularly, Sentinel-2A and 2B (S-2A and S-2B) in the optical domain and Sentinel-1A and 1B in the C-band microwave frequency (5.405 GHz, 5.6 cm) have been launched. The aim is to overcome these scale-related limitations by allowing image acquisitions with both good temporal and spatial resolutions under the same viewing angles (Ose et al., 2016). S-2A and S-2B, launched in 2015 and in 2017, that occupy the same orbit but 180° apart from each other, provide a temporal resolution of 10 days each and around 5 days with S-2A and S-2B together, reduced to 2–3 days over mid-latitudes regions. Spatial resolution of S-2 varies from 10 m to 60 m depending on the spectral band. SAR (Synthetic Aperture Radar) Sentinel-1A and 1B (S-1A and S-1B), launched in 2015 and 2016 respectively, that also occupy the same orbit, but separated by 180°, together offer a temporal resolution of about 3 days at the equator, >1 day at high latitude and about 2 days in Europe combining ascending and descending orbits. S-1 images may be available at a spatial resolution of 10 m in Interferometric mode (ESA, Sentinel-1 user guide). Temporal resolution of S-2 and S-1 are therefore comparable to the occurrence of phenological observations collected in the field over forest ecosystems, usually once or twice a week, and the spatial resolution of 10 m is also comparable to the size of adult forest tree crowns.

Typically, vegetation phenological metrics are derived from the analysis of time-series of spectral vegetation indices (SVI) in the optical domain. However, SVI are subject to varying degrees of uncertainty due mainly to cloud cover and cloud shadow contamination, which either introduces random noise that is difficult to correct or makes the data totally unavailable (Hird and McDermid, 2009; White and Wulder, 2013). Therefore, the temporal resolution of the satellite-based optical sensors is theoretical since the availability of data depends on sky conditions (Wang and Atkinson, 2018; Sudmanns et al., 2019). In comparison to optical remote sensing, the main advantage of SAR remote sensing in the microwave domain is its ability to pass through clouds with negligible attenuation. Temporal resolution is therefore maintained from year to year or from one region to another regardless of cloud conditions.

Due to these characteristics (spatial resolution, temporal resolution and low sensitivity to cloud conditions), S-1 SAR data is a good candidate as a proxy of phenology, but provided that it is sensitive enough to track phenological phases and that it can be interpreted in a way which is consistent with ground observations.

While the potential of S-2 for estimating forest phenology has been evaluated in many studies (Lange et al., 2017; Vrieling et al., 2018; Kowalski et al., 2020; Bolton et al., 2020), little is known about the potential of SAR data in general and S-1 in particular. The potential of S-1 has previously been assessed to monitor phenology, productivity and cultural practices in crops and meadows (Vavlas et al., 2020; Song and Wang, 2019; Stendardi et al., 2019), but at the exception of studies by Rüetschi et al. (2018) and Proietti et al. (2020), to the best of our knowledge no other studies which have compared phenological estimates derived from S-1 with field phenological observations in

deciduous forests. In Rüetschi et al. (2018), few field phenological observations were available and, as pointed out by the authors, the temporal resolution of used S-1 time-series (24 days) was not adequate for an accurate assessment. Proietti et al. (2020) clearly demonstrated the potential of S-1 for the detection of the phenology in beech stands. However, these two studies concerned only the spring phenological stage. In other studies, Dostálová et al. (2016, 2018) and Frison et al. (2018) analyzed S-1 time-series over deciduous and coniferous forest stands. However, these studies were limited to the analysis of the temporal patterns of the S-1 data and did not focus on their exploitation for the detection of phenological dates.

The overall aim of this work is to leverage available ground-based measurements over one deciduous forest site in order to quantitatively assess the potential of S-1 time series as a proxy of phenology, and to explore the potential mechanisms involved in the S-1 temporal variability. In this paper, our objective is to investigate the potential of time-series of S-1 A&B C-band dual-polarized (VV and VH) SAR images to describe the phenological patterns of a temperate deciduous forest, and to estimate the timings of the main spring and autumn phenological stages. To this aim, we compared S-1 based spring and autumn phenological estimates to in situ phenological observations by human observers and to estimates from alternative in situ indirect approaches including daily time-series of proximal NDVI (normalized difference vegetation index), daily time-series of LAI (Leaf Area Index) estimated from continuous radiation measurements and time-series of NDVI derived from S-2 A&B images. During the autumnal phenological stage, we also compared S-1 based phenological dates to temporal dynamics of litterfall monitored in the field.

2. Materials and methods

2.1. Site description

The study site is the Fontainebleau-Barbeau forest station (48°28′26″N, 2°46′57″E), located 53 km southeast of Paris (Fig. 1).
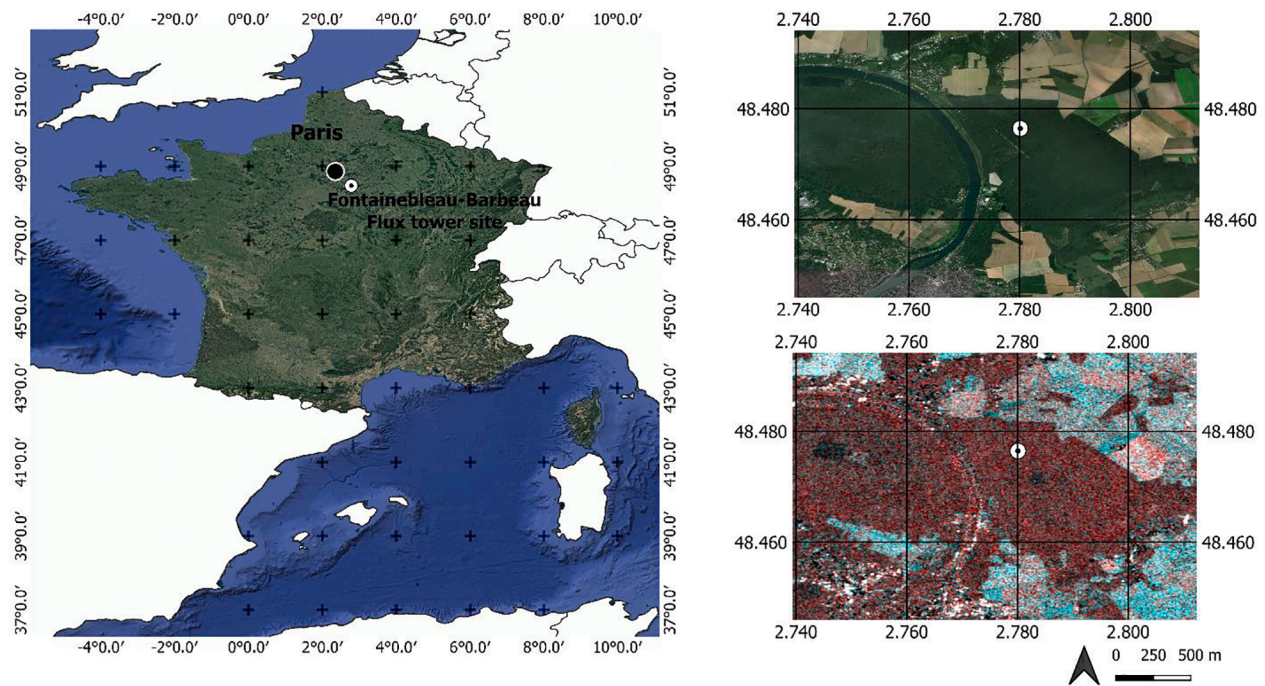
Briefly, Fontainebleau-Barbeau forest is mainly composed of sessile oak (*Quercus petraea* (Matt.) Liebl), with an understory of hornbeam (*Carpinus betulus* L.). The stand age is about 150 years and the dominant height of trees is 27 m. The average LAI of the stand, based on measurements using litter collection method over 2012–2018 period, is 5.8 m^2/m^2, ranging from 4.6 to 6.8 m^2/m^2 (Soudani et al. 2021). The topography is flat, and the ground elevation is about 103 m a.s.l. On this site which belongs to the pan-European ICOS Ecosystem network (Integrated Carbon Observation System, ICOS code FR-Fon), a 35-m high tower has been installed in 2005, measuring energy and matter (CO_2 and H_2O) exchanges between the vegetation and the atmosphere using the eddy-covariance (EC) technique. More details can be found in Delpierre et al. (2016) and at http://www.barbeau.u-psud.fr/index-fr.html.

2.2. Data

2.2.1. SAR Sentinel-1C-band time-series

Time-series of SAR Sentinel-1 (A&B) backscattering coefficient (σ^0) at VH and VV polarization were composed using the Google earth engine (GEE) (Gorelick et al. 2017). A total of 470 dual polarized (VV and VH) images covering the period from 01/01/2015 to 31/12/2019 were used. 225 scenes are in ascending orbit and 245 in descending orbit. Before September 2016 (day of year 278), S-1 time-series are composed of S-1A images only. All images, including S1-A and S1-B were acquired at relative orbits 59 in ascending orbit and 110 in descending orbit. The study site is practically located at the center of the intersection of the two orbits. The incidence angle at the study site was approximately 39° for all images.

The number of S-1 images used per year is 43 images in 2015, 74 in 2016, 119 in 2017, 117 in 2018 and 117 in 2019; thus an average of about 1 image every 8 days in 2015, 1 image every 5 days in 2016 and 1

Fig. 1. Fontainebleau-Barbeau forest location in France (48°28′26″N, 2°46′57″E). Bottom right panel: Sentinel-1 RGB composite with median VV/VH during the summer (15/06–31/08/2019) in red, median VV/VH during the winter (01/01–31/03/2019) in green and blue. (For interpretation of the references to colour in this figure legend, the reader is referred to the web version of this article.)

image every 3 days in 2017/2018 and 2019. As mentioned above, the number of images available in 2015 is low since only S-1A was operational. Images used are provided by European Union's Copernicus program and available in GEE in GRD (Ground Range Detected) format, in interferometric wide (IW) swath mode, already calibrated and *ortho-corrected* using the Sentinel-1 Toolbox at 10-m spatial resolution (https://developers.google.com/earth-engine/guides/sentinel1). Each image contains two layers of the backscattering coefficient σ_0 in VV and VH dual polarization converted in decibels unit (dB). Time-series of σ_0 were composed based on their means within a circular buffer of 50 m in radius, centered on the Fontainebleau-Barbeau EC flux tower (Fig. 1). The number of S-1 pixels within the buffer is about 78 pixels.

Means of VV and VH in dB unit over the plot were then used to determine VV/VH ratio as follows (Eq. (1)):

$$VV/VH(dB) = \sigma^0 VV(dB) - \sigma^0 VH(dB) \tag{1}$$

This implies calculating VV/VH as the arithmetic mean of VV/VH (dB) of all pixels within the plot. Indeed, at the plot scale, as mentioned above, phenological observations are made at the scale of individual trees. Then, the phenological date of budburst or senescence of the whole plot is an arithmetic mean of observed dates on individual trees within the plot. In our study, in order to build VV/VH time series to derive phenological metrics, we consider that the phenological information is carried by the average of VV/VH in dB unit over all pixels for a given date. An alternative procedure is to calculate the average intensity over all pixels within the plot and then apply the logarithmic transformation to convert average plot intensity into dB unit. For our purpose, this last procedure may be not relevant since the phenological date of the plot is determined from phenological dates of individual trees represented by pixels rather than by the phenological date obtained from an average pixel. However, in this case, we observe that the two procedures provide similar results. Deviations are 0.35 dB in VV, 0.38 dB in VH and 0.01 dB in VV/VH. This conclusion reflects the homogeneity of the plot since the deviation between the two procedures can be used as an index of plot homogeneity as shown in Woodhouse (2001). More details on the comparison of the two calculation procedures are

provided in S1, in supplementary material.

2.2.2. Sentinel 2 A & 2B time-series

A total of 284 Sentinel-2 (A&B) images (193 S-2A and 91 S-2B) from the S-2 L1-C TOA reflectance product, also provided by European Union's Copernicus program (https://developers.google.com/earth-engine/datasets/catalog/COPERNICUS_S2), were processed under GEE to generate NDVI time-series using bands 4 (red) and 8 (near infrared) over the period 2015–2019. The corresponding wavelengths are respectively 664.5 nm (S-2A)/665 nm (S-2B) for the red band and 835.1 nm (S-2A)/833 nm (S-2B) for the near infrared band. The NDVI was calculated per pixel and averaged over the same 50 m radius buffer as for S-1 A&B. The spatial resolution of the S-2 red and near infrared bands is 10 m and the number of pixels within the circular buffer is the same as for S-1 (78 pixels). Pre-filtering of cloudy pixels was performed using the QA60 flag, bits 10 and 11, which provide information about clouds and cirrus at the 60 m pixel scale. Only cloudy and cirrus-free pixels within the buffer were used in the calculation of NDVI. The number of S-2 images per year is 4 images in 2015, 11 in 2016, 17 in 2017, 28 in 2018 and 31 in 2019. From June 2015 to March 2017, only S-2A was operational, explaining the low number of images available for these two years. The year 2015 was excluded from the analysis due to the insufficient number of images.

2.2.3. In situ data

2.2.3.1. Field phenological observations. A detailed description of field phenological data is given in Denéchère et al. (2019), Delpierre et al. (2020) and Soudani et al. (2021). Briefly, phenological observations were conducted according to two complementary sampling protocols. The first protocol (hereafter *intensive*) protocol was conducted from 2015 to 2017 for both spring and autumn. In this protocol, temporal dynamics of spring (percentage of open buds) and autumn (percentage of colored and/or fallen leaves) phenological transitions were determined at tree level, on 30 to 66 trees from the early signs to the end of each phenological stage. The second protocol (hereafter *extensive*)

protocol was conducted in 2018 and 2019, during the spring phase only. In this protocol, we determined the date of budburst visually at the whole plot level surrounding the flux tower on about 100 oak trees. We considered that a tree had reached budburst when 50% of its crown showed open buds (corresponding to stage 7 of the BBCH scale). Budburst of the whole plot was reached when 50% of sampled trees have reached budburst. All observations were achieved using binoculars by three inter-calibrated observers, on a bi-weekly basis during the budburst (BB-OBS) and weekly during the senescence (LS-OBS). Hence the uncertainties are 3.5 days for BB-OBS and 7 days for LS-OBS.

2.2.3.2. Narrow-band NDVI data. The NDVI is calculated as follows (Eq. (2)):

$$NDVI = (NIR - R)/(NIR + R) \qquad (2)$$

R and NIR are radiances in the red (640–660 nm) and the near infrared (780–920 nm) bands, respectively. Radiances are measured using a laboratory made NDVI sensor. A description of this sensor and its use for estimating phenological metrics in various biomes is given in Soudani et al. (2012, 2021) and Hmimina et al. (2013). Briefly, the sensor is positioned at the top of the flux tower in the Fontainebleau-Barbeau forest, about 7 m above the canopy, pointing downwards and inclined about 20-30° from vertical and facing south to avoid the hot-spot effects in canopy reflectance when the viewing direction is collinear with the solar direction. The field of view of the sensor is 100° and the observed area is a few tens of m². Measurements are acquired continuously every half-hour. Noisy data, due mainly to rainfall and very low radiation conditions, were removed according to the procedure described in Soudani et al. (2012). Daily average of filtered NDVI data acquired between 10 h and 14 h (UT) is considered to minimize daily variations in solar angle.

2.2.3.3. Leaf area index LAI. For the different years, the maximum of leaf area index reached during the summer is determined directly using the litter collection method. 20 litter traps of 0.5 m² each were used according to the standard protocol adopted within the framework of the European ICOS Ecosystem network (Gielen et al. 2018). The litter collection during the autumn is carried out at a one-week time step, thus allowing, in addition to the determination of maximum LAI, the description of temporal dynamics of surface area of fallen leaves from the first fallen leaves until the end of the autumn season.

Continuous estimation of canopy LAI was also achieved by applying the Beer-Lambert law to continuous measurements of above and below canopy radiation.

The LAI was estimated as follows (Eq. (3)):

$$LAI = -log(PARt/PARin)/K \qquad (3)$$

log is the natural logarithm. PAR*in* is the incoming radiation measured above the forest canopy in the visible spectral region (400–700 nm) corresponding to the spectral range of PAR (Photosynthetically active radiation) measured using PAR sensors (PQS1, Kipp and Zonen, Finland). PAR*t* is the average transmitted radiation below the forest canopy in PAR spectral region over 15 sensors. These sensors, directed towards the sky, are installed in the area surrounding the EC flux tower to ensure a robust spatial sampling of the radiation transmitted through the canopy. Measurements are achieved at a half-hour time step, simultaneously with measurements of incoming PAR radiation. K is the coefficient of extinction, calculated following the expression given in Campbell and Norman (1998) (Eq. (4)):

$$K(\theta) = \frac{\sqrt{x^2 + tan(\theta)^2}}{x + 1.774(x + 1.182)^{-0.733}} \qquad (4)$$

θ is the sun zenith angle and x is a parameter that describes an ellipsoidal leaf angle distribution function (x = 1 for spherical distribution, x > 1

for planophile and x < 1 for erectophile leaves). In order to let K vary according to the seasonal variations of the solar angle, we only fixed the parameter x in Eq. (4). An average value of x parameter is estimated by the inversion of Eq. (3), based on average LAI maximum determined from the litter collection method and average transmitted PAR during the summer growing season. Estimated value of K is of about 0.67 during the leafy season. This value agrees with previous studies (Baldocchi et al. 1984). Finally, we note that K is estimated from the "true" average green LAI measured by the litter collection method, and thus it corrects for clumping effects and woody components.

2.3. Methods

2.3.1. Extraction of phenological metrics in spring and autumn from time-series

Six phenological metrics were extracted from time-series of S-1 VV/VH, in situ NDVI, S-2 NDVI, LAI and field phenological observations collected according to the intensive protocol. Three phenological metrics were also extracted from litterfall temporal dynamics. In order to compare the different vegetation proxies without possible methodological biases, the extraction of phenological estimates is carried out according to Zhang et al. (2003), Soudani et al. (2008) and Soudani et al. (2021). Briefly an asymmetric double sigmoidal function (ADS) was fitted to time-series according to the following equation (Eq. (5)):

$$Vp(t) = (w1 + w2) + \frac{1}{2}(w1 - w2)[\tanh(w3(t - u)) - \tanh(w4(t - v))] \qquad (5)$$

Vp (t) is the considered vegetation proxy (VV/VH, NDVI from S-2 and in situ measurements, LAI, % of open buds, % of colored and/or fallen leaves). t is the time (day of year). tanh is the hyperbolic tangent and w_1, w_2, w_3, w_4, u, v are the fitted parameters. ($w_1 + w_2$) is the *Vp* minimum in unleafy season. (w_1-w_2) is the total amplitude of the *Vp* seasonal cycle. u and v are the dates of the two inflection points when *Vp* increases during the spring (u) and decreases during the autumn (v). Six phenological markers are extracted from ADS fitted to data and named according to Klosterman et al. (2014): SOS, MOS and EOS for the start, middle, and end of leaf onset (budburst) in spring and SOF, MOF and EOF for the start, middle and end of leaf senescence in autumn (Fig. 2).

MOS and MOF correspond to u and v and are very close to 50% of the total amplitude of variation of *Vp*, in spring and autumn respectively.
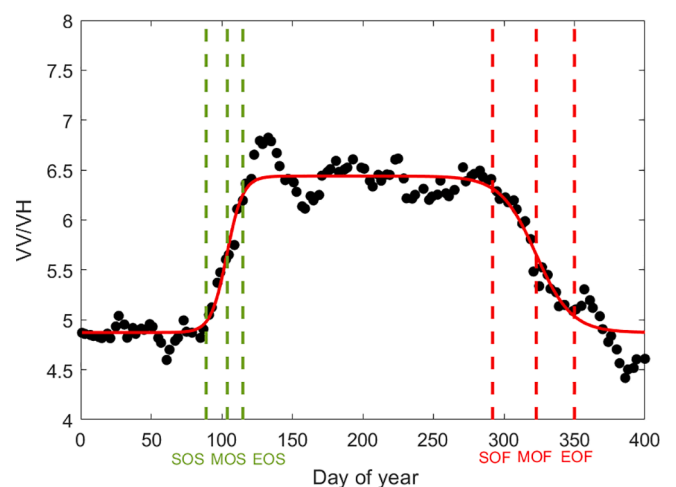
Fig. 2. Phenological markers extracted from ADS (asymmetric double sigmoid) function fitted to VV/VH time-series acquired in 2018 (filled circles and red curve). Vertical lines: in green, SOS, MOS and EOS are dates of start, middle and end of leaf onset in spring; in red, SOF, MOF and EOF are dates of start, middle and end of leaf senescence (colored and fallen leaves) in autumn. (For interpretation of the references to colour in this figure legend, the reader is referred to the web version of this article.)

SOS, EOS, SOF and EOF are determined numerically from the extrema of the third derivative of fitted ADS according to Zhang et al. (2003) and correspond approximately to 10% and 90% of total amplitude of *Vp* during the increase (SOS and EOS) and the decline (SOF and EOF) in canopy greenness in spring and autumn, respectively. Fitting of ADS to *Vp* time-series was done by minimizing the sum of squares of differences between fitted (Eq. (5)) and measured *Vp*. To better constrain the fitting at the end of the leafy season, each year of data was extended to the end of January of the following year. Thus, potentially, each time-series is composed of 396 days instead of 365 days. All phenological dates were determined using the ADS function fitted to the data (Fig. 2), except for SOF and EOF dates determined from litterfall temporal dynamics. For litterfall time-series, MOF is determined using the ADS function but SOF and EOF are determined directly from the data, due to the poor quality of the fit of ADS function on both sides (before the start and after the end of the litterfall). SOF and EOF are, respectively the dates corresponding approximately to 10% and 90% of the total litterfall. Finally, note that, in order to remove noise, time-series of VV/VH ratio were filtered using the Savitzky-Golay filtering method under the MATLAB® environment (www.mathworks.com).

2.3.2. Statistical analysis

The performance of VV/VH time-series to predict phenological events in spring and autumn was evaluated with respect to the field phenological observations using the mean bias error (MBE) and the mean absolute deviation (MAD) between estimated (P_i) and observed dates (O_i) for the different years (N), calculated as follows (Eq. (6) and Eq. (7)):

$$MBE = \frac{1}{N}\sum_{i=1}^{N}(P_i - O_i)$$ (6)

$$MAD = \frac{1}{N}\sum_{i=1}^{N}|(P_i - O_i)|$$ (7)

Statistical significance is determined at 5% probability level using one-tailed and two-tailed Student's *t*-test for comparison of means of σ^0VV, σ^0VH and VV/VH between ascending and descending orbits and between the leafy growing season and winter dormancy season. Statistical analysis was done using the R software (R Core Team, 2018)

3. Results

3.1. SAR Sentinel-1 VV/VH time-series

S-1 VV/VH time-series are shown in Fig. 3. σ^0 in VV and VH polarization in ascending and descending orbits are shown in Figure S2, in supplementary material. Using S-1 original data (before filtering, Figure S2 for more details), the coefficient of backscattering σ^0 is on average, over all years, about −8.54 dB ([−10.73, −5.07]) in VV polarization and about −14.40 dB ([−17.48, −10.45]) in VH. Considering both ascending and descending orbits, differences in means of VV and of VH are about 0.5 dB in both polarization modes but are statistically significant. However, the difference between means of VV/VH in ascending and descending orbits (about 0.1 dB) is not significant (P < 0.34). For this reason, S-1 data acquired at the two orbits are considered without distinction in the following.

Fig. 3 shows that S-1 VV/VH time-series reproduce the seasonal patterns of canopy structure observed in deciduous forests. Four phases can be distinguished: a winter phase with low VV/VH values, a rapid transition phase during spring when VV/VH increases quickly, a plateau during the main growing season in summer and a fourth phase of VV/VH decline which coincides with the phase of leaf senescence and leaf fall. In comparison with the backscattering coefficients σ^0VH or σ^0VV, the VV/VH ratio is more dynamic and seems to be driven by VH more than by VV polarization (Figure S2).

Indeed, the backscatter coefficient σ^0VH decreases during spring phenological transitions, and remains relatively stable during the summer for which LAI remains stable and increases again during autumn phenological transition (Figure S2). Between its winter maximum and summer minimum, σ^0VH varies on average from −13.36 dB (standard deviation 0.871 dB) in winter [doy 330–98 next year] to −15.16 dB (standard deviation 0.851 dB) in summer [doy 128–270]. The decrease is of 1.80 dB, but σ^0VH is highly significantly lower in summer than in winter (P < 0.001, one-sided *t*-test). In vertical polarization, σ^0VV decreases from −8.43 dB (0.732 dB) in winter to −8.51 (0.710 dB) in summer (Figure S2). The decrease is only about 0.15 dB but is statistically significant at 5% (P < 0.048). In the VV/VH, driven mainly by changes in σ^0VH, the average increases from 4.93 dB (0.77 dB) in winter to 6.56 dB (0.79 dB) in summer. Also, VV/VH is very significantly higher in summer than in winter (P < 0.001, one tailed *t*-test).
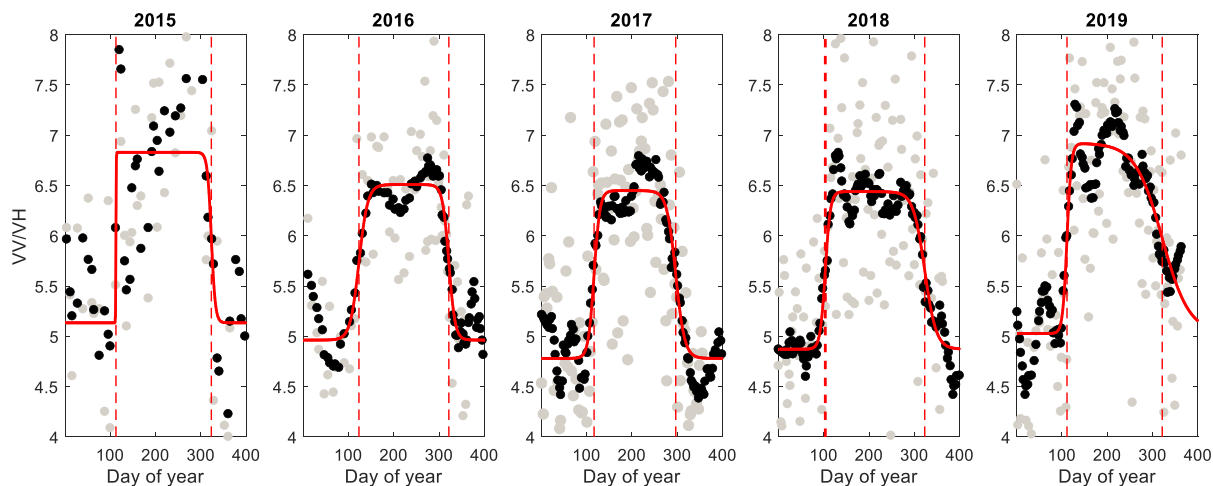
Fig. 3. Sentinel-1 VV/VH time-series (dB): grey circle: original data; black circle: data smoothed using a Savitzky-Golay filter; continuous red curve: asymmetric double sigmoid function (ADS) fitted to VV/VH smoothed data. Red vertical bars: estimated phenological transition (MOS and MOF) dates from VV/VH time-series based on ADS function. (For interpretation of the references to colour in this figure legend, the reader is referred to the web version of this article.)
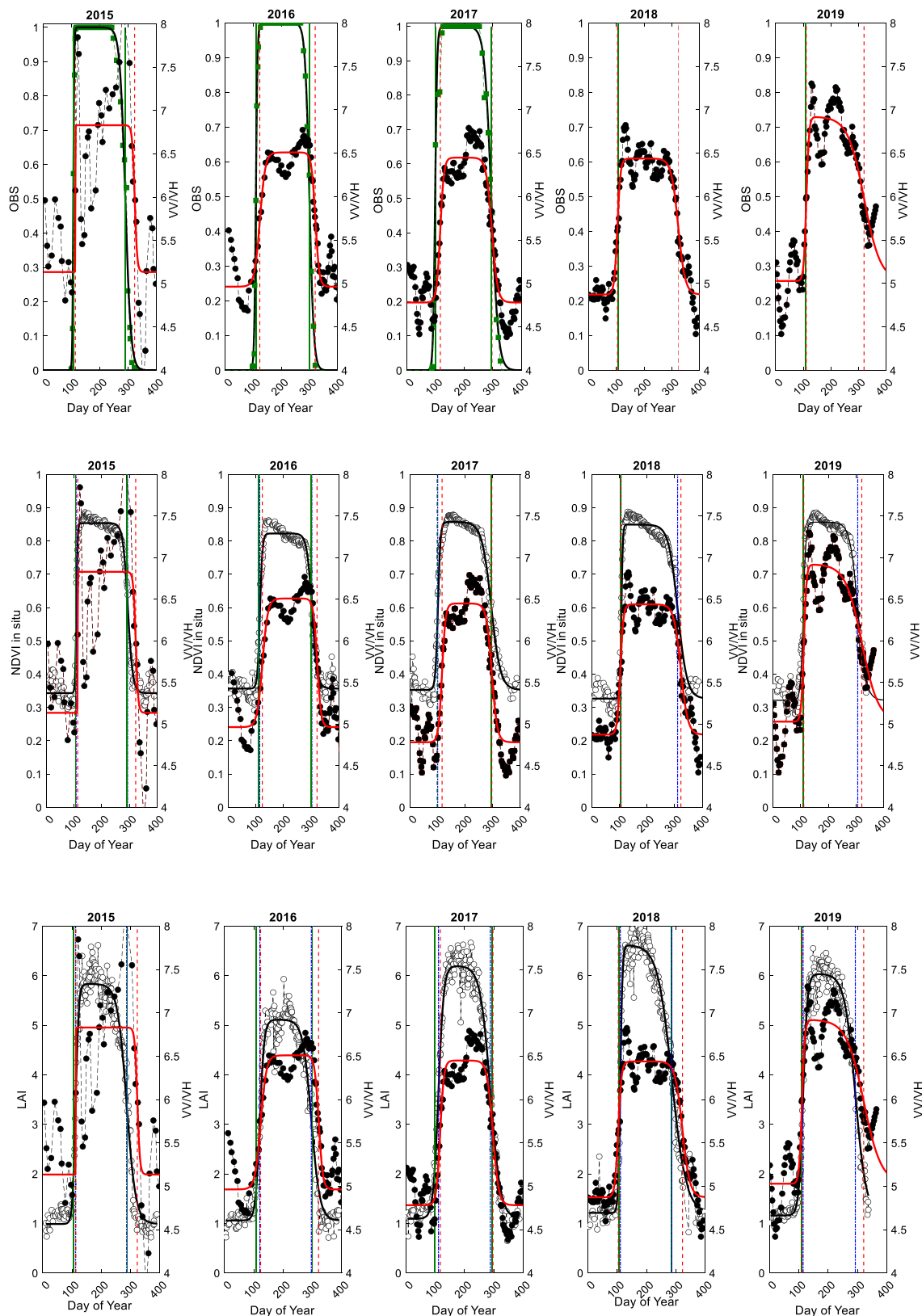
Fig. 4. Sentinel-1 VV/VH time-series for all subplots (black filled circles – red continuous curve – right axis). Empty circles – left axis: from top to bottom – time-series of field phenological observations (OBS from intensive protocol on 2015–2017), ground-based NDVI, Leaf Area Index (LAI), Litterfall in autumn and Sentinel 2 NDVI. Vertical bars: observed phenological transition dates in green (OBS from intensive and extensive protocols); estimated MOS and MOF phenological transition dates based on ADS function using VV/VH time-series in red and predicted phenological dates from in situ NDVI, LAI, S-2 NDVI (gray circle – removed using SG filter; empty circle – used) and litterfall in blue. (For interpretation of the references to colour in this figure legend, the reader is referred to the web version of this article.)
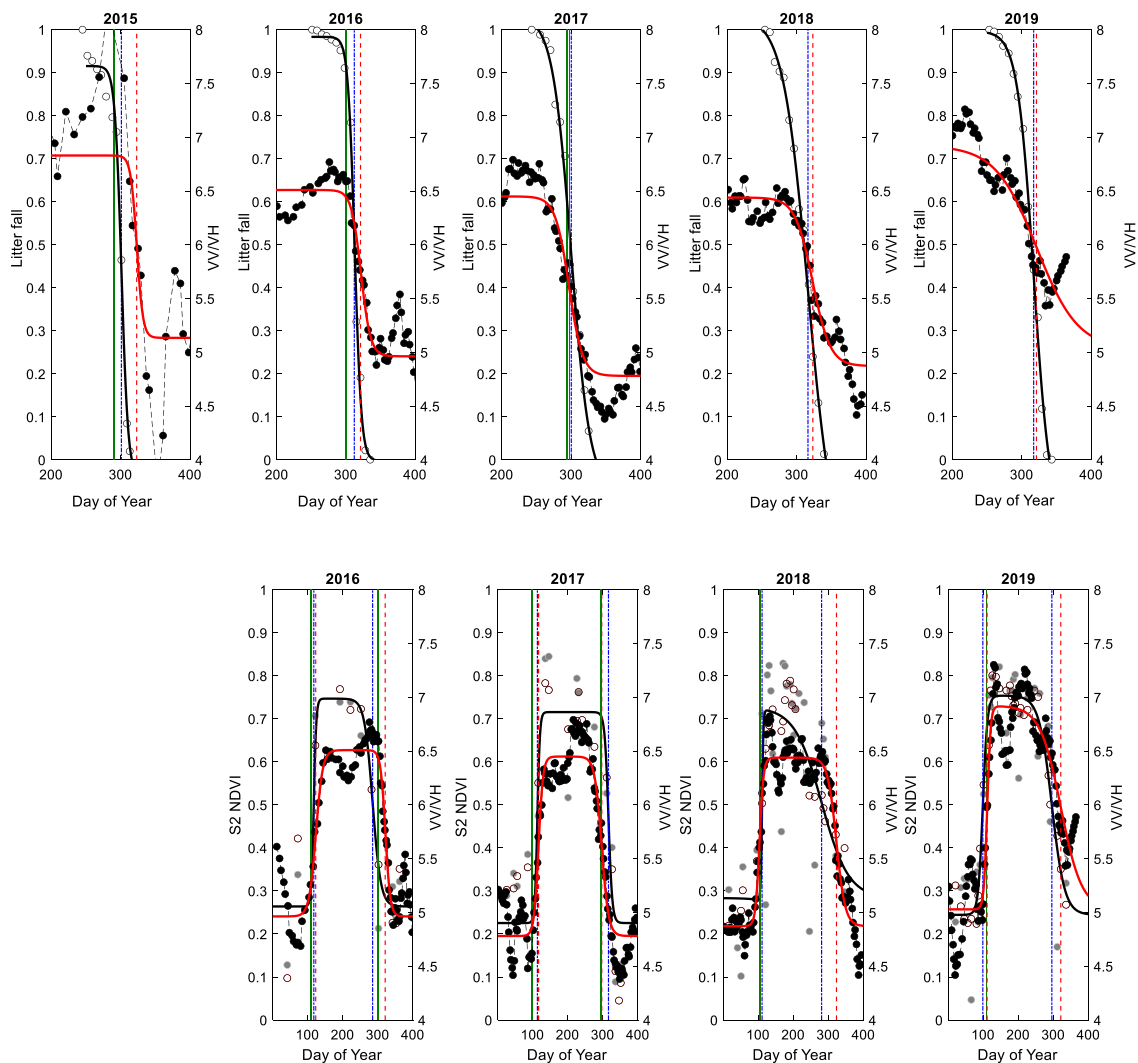
Fig. 4. (*continued*).

3.2. Phenological metrics derived from SAR Sentinel-1 VV/VH time-series

The temporal dynamics of VV/VH strongly co-vary with the canopy phenological cycle, as assessed through various vegetation proxies (Fig. 4). Summary statistics are given in Table 1 and estimated dates by year and for the six phenological metrics (SOS, MOS, EOS in spring and SOF, MOF and EOF in autumn) are given in Supplementary Material S3.

Fig. 5 illustrates the interannual variations in estimated budburst (MOS) and senescence dates (MOF) for the different approaches.

During the spring transition phenological stage, and based on MOS criterion, VV/VH time-series lag about 8 days behind the observed budburst date (MBE and MAD, 8 and 8.5 days respectively; Fig. 5a). This lag with observed budburst dates is similar to the lag of MOS retrieved from LAI time-series (MBE and MAD of about 8.5 days) and is slightly lower by about 1.5 days in comparison to the lag between MOS estimates retrieved from S-2 NDVI time-series (for S-2 NDVI, MBE and MAD of about 5 days and 10 days, respectively). The best estimates are obtained using in situ NDVI time-series for which MBE and MAD are about 2 days. During the autumnal phenological phase, for the three years for which continuous field observations are available, VV/VH time-series provide estimates which are approximately 20 days later than the observed dates (Fig. 5b) while the differences are of the order of 2 to 4 days between the

Table 1
Summary statistics (mean and min–max of day of year) of observed and estimated phenological dates. SOS, MOS and EOS for the start, middle, and end of season in spring and SOF, MOF and EOF for the start, middle and end of season in autumn. (*) For field phenological observations, MOF is determined for the five years from the extensive protocol. SOS, EOS, SOF, MOF and EOF, are determined for years 2015 to 2017 using the intensive protocol.

|	Onset of greenness and leaf expansion			Leaf senescence and fall		
	SOS	MOS	EOS	SOF	MOF	EOF
Phenological observations (*)	97 (89–102)	105.5 (99–109)	110.5 (108–115)	272 (267–282)	294.5 (290–300)	316.5 (321–321)
S-1 VV/VH	100 (89–110)	113.5 (104–123)	124.5 (113–144)	287 (252–312)	317 (297–323)	345 (318–388)
In situ NDVI	98 (90–103)	107.5 (101–113)	115.5 (111–123)	270 (255–280)	301 (293–311)	331.5 (314–349)
S-2 NDVI	102.5 (83–115)	110 (99–118)	119114–124	252 (192–303)	294 (281–316)	338 (320–368)
LAI	98.5 (90–103)	114 (111–120)	128 (119–137)	248.5 (231–263)	290 (287–296)	330.5 (322–341)
Litterfall	–	–	–	281 (266–298)	309 (300–317)	323 (309–331)

Budburst
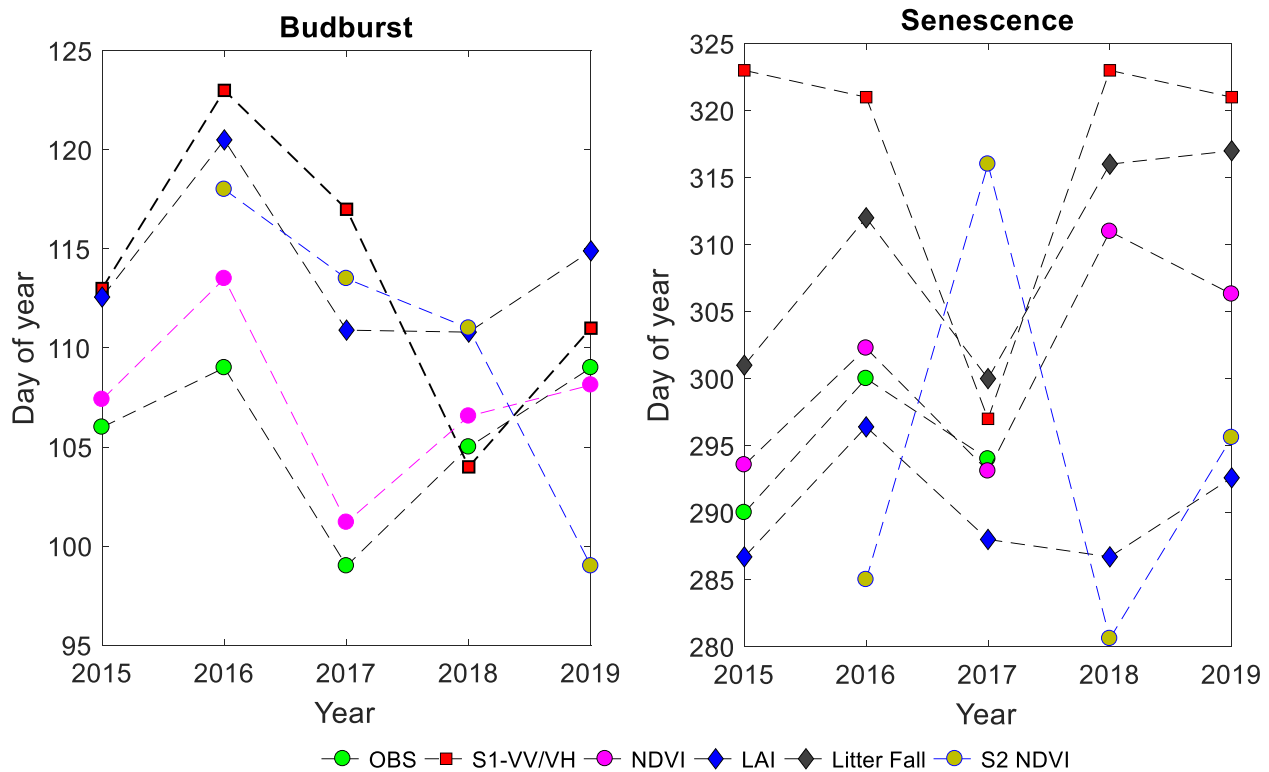
Senescence

Fig. 5. Spring and autumn phenological dates extracted from VV/VH time-series: Average dates (day of year) of budburst (a- left) and senescence (b- right) based on MOS and MOF, respectively.

observations and estimates based on in situ NDVI and LAI, respectively. Interestingly, MOF derived from VV/VH differs by 7 days on average from MOF determined from litterfall time-series. Between S-1 and S-2 based estimates, MBE and MAD are respectively of − 4 days (S-2 based estimates later) and 7 days during the spring and −20 days (S-2 earlier) and 30 days in autumn (Fig. 5b, Table S3).

These differences between VV/VH estimates and those obtained using field phenological observations and the other alternative methods depending on whether we consider the spring or autumnal phenology reflect different relationships between the temporal dynamics of the VV/VH signal and canopy properties. Fig. 6 illustrates the relationships between VV/VH, LAI and in situ NDVI during the four phenological stages: winter dormancy period, spring leaf emergence and expansion stage, summer growth stage, and autumnal leaf senescence and fall. Four years are shown, from 2016 to 2019, for which more S-1 data are available and phenological estimates are more robust.

Fig. 6 shows a positive relationship between VV/VH and both NDVI and LAI. These relationships are not unique and depend on the phenological stage considered. A hysteresis phenomenon can be noted as the VV/VH trajectories are not identical during the increase and the decrease in canopy leaf area as described using LAI or NDVI, during spring and autumn, respectively. For the same NDVI (or LAI), VV/VH is higher during the fall phase than during the spring phase.

4. Discussion

Examination of S1 time series built from the raw data are highly noisy and filtering was required to extract phenological metrics (Fig. 3). The sudden and large variations of VV/VH signal may be due to rain events. Indeed, C-band sensitivity to precipitations intercepted and stored by the canopy during data acquisition day has been shown in previous studies from measurements (Benninga et al., 2019; El Hajj et al., 2016; Proisy et al., 2000) and from model-based simulations (Jong et al., 2000). VV/VH time series were composed by combining data

acquired from two distinct ascending and descending orbits, with two similar incidence angles but in two opposite viewing directions. However, the noise due to the combination of the two orbits is negligible. Indeed, as mentioned above, differences in VV/VH between the two orbits are very small, about 0.1 dB on average, and statistically not significant. This result also reflects the spatial homogeneity of the forest canopy structure, particularly in terms of trees height, and the absence of large gaps, which can cause shadowing effects depending on the viewing direction (Eriksson et al. 2012; Bouvet et al. 2018; Rüetschi et al. 2019).

As also shown in Figure S2, σ^0VH is more sensitive to the phenological cycle observed in deciduous forests while the temporal profile of σ^0VV remains relatively stable throughout the year. Indeed, σ^0VV difference between the leafy growing season and winter dormancy season, is about 0.15 dB. Although statistically significant, this difference can be considered as negligible since the reported radiometric accuracy of S1-A and S1-B at VV and VH polarization was defined to be 1 dB for all operations modes (Schmidt et al. 2018). This difference is also smaller than the radiometric uncertainty of about 0.48 dB on average estimated on invariant targets consisting of two evergreen forests and bare soil in El Hajj et al. (2016) using S1-A data. In another study (Benninga et al. 2019), radiometric uncertainty estimated on several land cover types including forests, meadows, and crops, was between 0.85 dB and 0.30 dB in VV polarization and between 0.89 dB and 0.36 dB in VH polarization depending on the considered area over which the σ^0 data are averaged, ranging from 0.25 ha to 10 ha, and according to an inverse square root decay. On the other hand, σ^0VH shows a significant decrease of about 1.80 dB on average during summer growing season in comparison to winter dormancy period. This result agrees with the studies of Rüetschi et al. (2018), Dostálová et al. (2016, 2018), Frison et al. (2018) and Proietti et al. (2020) in which they observed a lower backscattering coefficient in the S-1 VH polarization in summer than in winter in temperate deciduous forests. Dostálová et al. (2016, 2018) observed a clear decrease in S-1 VH signal during the spring and an increase during
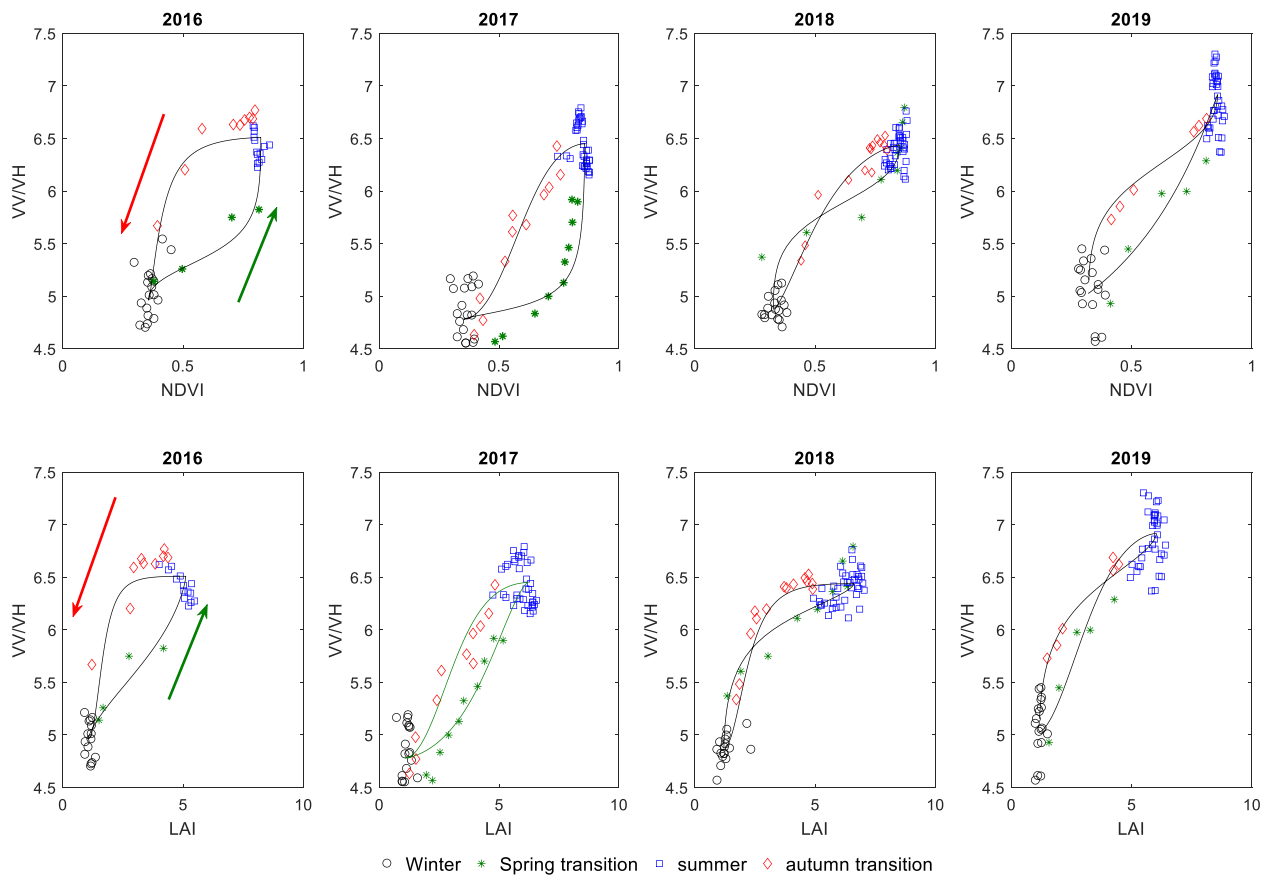
Fig. 6. Relationships between VV/VH (dB) and in situ NDVI (top) and LAI (bottom) according to the phenological stage. Symbols are measurements: winter (day of year: 330–98 of the next year) in black circles; spring transition (day of year 98–128) in green stars; summer growing season (day of year 128–270) in blue square; autumn transition (day of year 270–330) in red diamond. Continuous curves are predicted values using the ASD function. Red and green arrows give the directions of VV/VH trajectories during the autumn (red) and spring (green) phenological stages, respectively. (For interpretation of the references to colour in this figure legend, the reader is referred to the web version of this article.)

the senescence transition stage in the range of 0.5 to 2 dB in broadleaf forests of oak, beech, maple and birch trees. Similar results were obtained by Frison et al. (2018) over the whole Fontainebleau forest massif to which the Fontainebleau-Barbeau forest (our study site) belongs. The authors observed a decrease in σ^0VH in spring from −12.5 to −15 dB, while σ^0VV remains relatively stable. Rüetschi et al. (2018) and Dostálová et al. (2016, 2018) explained the decrease in VH backscatter during the growing season, when leaf biomass is at its maximum, by a lower contribution of branches to backscattering, considered more reflective than leaves in C-band, and by a lower contribution of soil masked by foliage.

The sensitivity of σ^0VH and VV/VH to phenology shown in our study (Figs. 3 and S2), characterized by a decrease of the former and an increase of the latter during the summer, is different from what can be observed on various types of crops as shown in many studies (Veloso et al., 2017; Khabbazan et al., 2019; Stendardi et al., 2019; Dostálová et al., 2018) in which an increase in σ^0VH signal and a decrease in VV/VH ratio when biomass increases in maize, soybean, sunflower, potatoes crops and in alpine meadows. In those studies, the increase of σ^0VH backscattering was explained by the increase in vegetation volume scattering acting as the main backscattering mechanism.

As underlined above, VV/VH ratio is more dynamic than σ^0VH and σ^0VV and better describes the seasonal dynamics of the canopy (Figs. 3 and S2). VV/VH is also known to be more stable and able to reduce the soil moisture and soil-vegetation interactions effects (Vreugdenhil et al., 2018; Veloso et al., 2017). As shown in Fig. 4, S-1 VV/VH reproduces the annual cycle of phenological events observed in deciduous forests with varying degrees of accuracy.

The estimated phenological dates using MOS marker from VV/VH time-series are in agreement with the observed dates, with a positive bias of about 8 days during spring (Fig. 5a). This result confirms the findings of Proietti et al. (2020). Proietti et al., using γ^0 VH instead of σ^0VH after topographic normalization, showed a strong potential of VH band from S-1 images for the detection of spring phenology with an uncertainty <4 days as soon as the first leaves are visible in beech stands. To our knowledge, the study of Proietti et al. (2020) is the first study that accurately assessed the potential of S-1 for estimating forest phenology. Nevertheless, it should be noted that this study was only limited to the spring season and the estimates of phenological dates from VH signals that are closest to in situ observations were determined visually. Our study confirms the findings of Proietti et al. (2020) about the potential of S-1 for estimating spring forest phenology and shows that this potential is also valid during senescence phase. We also extend the comparison of the estimates provided by S-1, not only to in situ observations, but also to estimates provided by other commonly used proxies of forest phenology (NDVI, LAI and litterfall).

As mentioned above, in our study, the MOS estimates of the spring phenological transition, are positively biased by about 8 days. A similar bias is obtained using the LAI time-series. Indeed, during the spring transition phase (Fig. 4), we observe that time-series of VV/VH overlap with those of LAI but deviate very significantly during the autumnal phenological phase. Indeed, while during the spring phase, the patterns of VV/VH, LAI and NDVI from in situ and S-2 data, are relatively close, they deviate very strongly during the senescence phase causing large differences in the estimation of senescence dates (Fig. 4). During this phase, VV/VH decay seems to follow more closely the temporal

dynamics of litterfall than the LAI or NDVI decay. During the autumn, temporal patterns of VV/VH are positively shifted with respect to those of LAI (estimates derived from VV/VH later). It can also be noted that temporal patterns of litterfall are also positively shifted in comparison to temporal patterns of LAI estimated from transmitted PAR. The average bias between estimates of the senescence date decreases from about 27 days between VV/VH and LAI to about 7 days between VV/VH and litterfall. During the senescence and compared to in situ and S-2 NDVI, VV/VH provides estimates that are generally later, between 4 and 30 days, with an average bias of 17 days compared to in situ NDVI and between −19 and 42 days and an average bias of 20 days with S-2 NDVI.

These results show that the relationships between VV/VH and LAI or NDVI are not stable but depend on the phenological stage considered. For the same LAI or NDVI, the VV/VH signal is generally weaker during the spring phenological stage than during senescence (Fig. 6). This implies that the canopy characteristics that modulate these variables are different. During spring, the concomitance of VV/VH increase with the increase of LAI, and to a lesser extent with NDVI, reflects the sensitivity of VV/VH, and particularly VH, to leaf emergence and expansion. Leaf area development and growth act both in terms of number and geometrical properties of scattering elements composed of leaves and young twigs, changes in their dielectric properties especially through leaf water content and by masking the contribution of trunks, branches, and soil. It is very likely that this last mechanism is the most important because trees of the Fontainebleau-Barbeau forest are about 150 years old and the contribution of the woody parts is expected to play a major role in winter and to decrease as LAI increases during the spring. The masking of the contribution of branches and trunks when LAI increases is all the more true since the studied forest plot has a dense canopy, with an LAI of about 5.8 m^2/m^2 on average. The canopy being closed, the backscattering signal, especially in VH band, is essentially sensitive to leaves, twigs and small branches in the upper layers of the canopy and the effect of soil may be considered negligible as shown in previous studies (Omar et al., 2017; Lucas et al. 2004; Ahern et al. 1993).

During the spring phenological stage, foliage development and expansion also modulate NDVI and LAI very strongly although they also depend on canopy structure and leaf structural and biochemical characteristics. During the senescence phase, the onset of VV/VH decline, estimated from the SOF criterion, is later than for NDVI and LAI and practically synchronous with litterfall. NDVI decreases before leaf fall due to leaf yellowing and browning that characterize autumn leaf senescence. During this period, in addition to the decrease in leaf chlorophyll content which is the main cause of the decrease in NDVI, leaf water content and leaf mass also decreased as shown in previous studies (Yang et al., 2016; Yang et al., 2017; Meerdink et al., 2016). LAI, estimated in this study from transmitted radiation, also decreases earlier, probably due to an increase of canopy transmissivity caused by a decrease in leaf chlorophyll content during this period. Therefore, VV/VH seems to depend much more on the amount of scattering elements (leaves, twigs, branches and trucks) which is better described by litterfall than by NDVI or LAI.

As stated above, while for various types of crops, many studies have shown a positive relationship between VH backscatter coefficient in C-band and LAI or NDVI (Vreugdenhil et al. 2018; Mandal et al., 2019; Wang et al., 2019; Stendardi et al. 2019), our results show that, in deciduous forests, these relationships are inverted. Temporal dynamics of LAI and NDVI in spring is accompanied by a decrease in VH and an increase of VV/VH ratio. As mentioned above, this pattern reflects the preponderant role played by trunks and branches in the backscatter in VH cross-polarization. In forest stands, the increase in LAI that accompanies budburst and leaf expansion phases of spring masks the woody parts and causes a decrease in the VH backscatter. For crops, vegetation growth and development are accompanied by an increase in VH backscatter due to a greater contribution from vegetation volume and an attenuation of the contribution from soil as reported in Vreugdenhil et al. (2018) and Stendardi et al. (2019).

5. Conclusion

Time-series of Sentinel-1 A and B backscattering coefficients were used to characterize the seasonal phenological cycles in a temperate deciduous forest over five years. While the backscattering coefficient in vertical polarization ($\sigma^0 VV$) remains relatively stable over the seasons, the backscattering coefficient in cross-polarization ($\sigma^0 VH$) responds significantly to the seasonal vegetation cycle, with a behavior that is opposite to what is usually observed on various crops. $\sigma^0 VH$ decreases during spring simultaneously with spring budburst and leaf expansion, reaches a minimum during the main growing season when canopy leaf area is at its maximum and increases again simultaneously with leaf fall. The observed $\sigma^0 VH$ seasonal amplitude is 1.8 dB on average. S-1 time-series of VV/VH ratio provides a good description of the seasonal vegetation cycle, allowing the extraction of spring and autumn phenological metrics and a quantitative comparison with ground-based estimations. Estimates of budburst dates in spring differ by approximately 8 days on average from field phenological observations. During the senescence phase, the estimates provided by VV/VH are late by about 20 days in comparison to field phenological observations and deviate significantly by about two to four weeks from the estimates provided by in situ NDVI, S-2 based NDVI and LAI time-series. While during the spring, temporal pattern of VV/VH correlates well with LAI and NDVI, during senescence, it is better explained by the dynamics of litterfall. The deviation between VV/VH and litterfall-based senescence estimates is reduced to about one week. These deviations are in line with the ones obtained using optical remote-sensing and highlight the potential of the VV/VH ratio to track deciduous forest phenology, notably under cloudy conditions. While the present work focuses on one site and a limited number of years notably due to the short span presently covered by the S-1 constellation, this approach should be extended across a network of observation sites in order to systematically assess the VV/VH ability to track phenological stages.

A hysteresis phenomenon is observed on the relationships between VV/VH and NDVI or LAI. For the same LAI or NDVI, the response of VV/VH is lower during canopy foliage increase in spring than during leaf senescence and fall in autumn. These relationships are not unique and lead to the conclusion that the mechanisms involved in the seasonality of VV/VH signal are different according to the phenological stage considered. This behavior can be explained by the preponderant contribution of woody parts in VH polarization backscattering, which decreases as the forest canopy becomes more and more closed during spring and summer and increases again during leaf senescence and fall in autumn. The hysteresis phenomenon shows that attenuation of $\sigma^0 VH$ signal by canopy foliage appears to be less important during spring and early summer than during senescence. This may be caused by two opposing mechanisms: a significant role of water content of canopy foliage during the spring which has the effect of causing an increase of $\sigma^0 VH$ and the role of foliage, which masks the woody components, and has an opposite effect of causing a decrease in $\sigma^0 VH$ (less contribution of woody components). This last mechanism appears to be preponderant since $\sigma^0 VH$ decreases during the spring transition as shown in this study but also in previous studies. During the senescence, the strong relationship between the $\sigma^0 VH$ increase and the opening of the canopy caused by litterfall suggests that the masking role played by foliage is also dominant. These results show that the interpretation of S-1 signals over deciduous forest canopies or their use for classification without or after fusion with optical data must be carried out with great care due to the temporal variability of the contributions of the different canopy components associated with the seasonal phenological cycle. This conclusion is particularly important in the context of wide-ranging efforts to track ecosystems phenology through remote sensing, as it implies the need for more studies across diverse ecosystems exhibiting diverse structural properties and phenological cycles. The use of physical approaches based on radar backscatter models in forest canopies will have the advantage of allowing a better understanding and evaluation of the

contributions of the different ecosystem components, including soil and vegetation cover, in the measured signal. It will also provide useful information to better establish the correspondence between indirect phenological metrics predicted from the S-1 time-series and field phenological observations. In this context, the proposed approach leveraging ground-based phenological observations which are routinely made across observation networks such as the Phenocam network (Richardson et al. 2018) could be used to quantitatively assess the link between S-1 signals and phenological metrics across a wide range of ecosystems and climates.

Author contribution

Declaration of Competing Interest

The authors declare that they have no known competing financial interests or personal relationships that could have appeared to influence the work reported in this paper.

Acknowledgments

References

Ahern, F.J., Leckie, D.fJ., Drieman, J.A., 1993. Seasonal changes in relative C-band backscatter of northern forest cover types. IEEE Trans. Geosci. Remote Sens. 31 (3), 668–680.

Baldocchi, D.D., Matt, D.R., Hutchison, B.A., McMillen, R.T., 1984. Solar radiation within an oak-hickory forest: an evaluation of extinction coefficients for several radiation components during fully leafed and leafless periods. Agric. For. Meteorol. 32, 307–322.

Benninga, H.J.F., van der Velde, R., Su, Z., 2019. Impacts of Radiometric Uncertainty and Weather-Related Surface Conditions on Soil Moisture Retrievals with Sentinel-1. Remote Sens. 11, 2025.

Bolton, D.K., Gray, J.M., Melaas, E.K., Moon, M., Eklundh, L., Friedl, M.A., 2020. Continental-scale land surface phenology from harmonized Landsat 8 and Sentinel-2 imagery. Remote Sens. Environ. 240, 111685.

Bouvet, A., Mermoz, S., Ballère, M., Koleck, T., Le Toan, T., 2018. Use of the SAR Shadowing Effect for Deforestation Detection with Sentinel-1 Time Series. Remote Sens. 2018 (10), 1250.

Campbell, G.S., Norman, J.M. 1998. The Light Environment of Plant Canopies. In: An Introduction to Environmental Biophysics. Springer, New York, NY0.

Gielen, B., Acosta, M., Altimir, N., et al., 2018. Ancillary vegetation measurements at ICOS ecosystem stations. Int. Agrophys. 10, 645–664.

Delpierre, N., Berveiller, D., Granda, E., Dufrêne, E., 2016. Wood phenology, not carbon input, controls the interannual variability of wood growth in a temperate oak forest. New Phytol. 210, 459–470.

Delpierre, N., Soudani, K., Berveiller, D., Dufrêne, E., Hmimina, G., Vincent, G., 2020. "Green pointillism": detecting the within-population variability of budburst in temperate deciduous trees with phenological cameras. Int. J. Biometeorol. 64, 663–670.

Denéchère, R., Delpierre, N., Apostol, E., Berveiller, D., Bonne, F., Cole, E., Delzon, S., Dufrêne, E., Gressler, E., Jean, F., Lebourgeois, F., Liu, G., Louvet, J., Parmentier, J., Soudani, K., Vincent, G., 2019. The within-population variability of leaf spring and autumn phenology is influenced by temperature in temperate deciduous trees. Int. J. Biometeorol. 65, 369–379.

Dostálová, A., Milenkovic, M., Hollaus, M., Wagner, W., 2016. Influence of forest structure on the Sentinel-1 backscatter variation—Analysis with full-waveform lidar data. In: Proceedings of the ESA Living Planet Symposium, Prague, Czech Republic, 9–13 May 2016.

Dostálová, A., Wagner, W., Milenković, M., Hollaus, M., 2018. Annual seasonality in Sentinel-1 signal for forest mapping and forest type classification. Int. J. Remote Sens. 1–23.

El Hajj, M., Baghdadi, N., Zribi, M., Angelliaume, S., 2016. Analysis of Sentinel-1 Radiometric Stability and Quality for Land Surface Applications. Remote Sens. 2016 (8), 406.

ESA – European Space Agency Website: https://sentinel.esa.int/web/sentinel/user-guides/sentinel-1-sar/revisit-and-coverage.

Eriksson, L.E.B., Fransson, J.E.S., Soja, M.J., Santoro, M., 2012. Backscatter signatures of wind-thrown forest in satellite SAR images. In: IEEE International Geoscience and Remote Sensing Symposium, pp. 6435–6438.

Fisher, J.I., Mustard, J.F., Vadeboncoeur, M.A., 2006. Green leaf phenology at Landsat resolution: Scaling from the field to the satellite. Remote Sens. Environ. 100, 265–279.

Frison, P.-L., Fruneau, B., Kmiha, S., Soudani, K., Dufrêne, E., Le Toan, T., Koleck, T., Villard, L., Mougin, E., Rudant, J.-P., 2018. Potential of Sentinel-1 Data for Monitoring Temperate Mixed Forest Phenology. Remote Sens. 2018 (10), 2049.

Gorelick, N., Hancher, M., Dixon, M., Ilyushchenko, S., Thau, D., Moore, R., 2017. Google Earth Engine: Planetary-scale geospatial analysis for everyone. Rem. Sens. Env. 202, 18–27.

Hird, J.N., McDermid, G.J., 2009. Noise reduction of NDVI time series: An empirical comparison of selected techniques. Remote Sens. Environ. 113, 248–258.

Hmimina, G., Dufrene, E., Pontailler, J.-Y., Delpierre, N., Aubinet, M., Caquet, B., de Grandcourt, A., Burban, B., Flechard, C., Granier, A., Gross, P., Heinesch, B., Longdoz, B., Moureaux, C., Ourcival, J.-M., Rambal, S., Saint-André, L., Soudani, K., 2013. Evaluation of the potential of MODIS satellite data to predict vegetation phenology in different biomes: An investigation using ground based NDVI measurements. Remote Sens. Environ. 132, 145–158.

Jong, J.D., Klaassen, W., Ballast, A., 2000. Rain storage in forests detected with ERS tandem mission SAR. Remote Sens. Environ. 72, 170–180.

Khabbazan, S., Vermunt, P., Steele-Dunne, S., Ratering Arntz, L., Marinetti, C., van der Valk, D., Iannini, L., Molijn, R., Westerdijk, K., van der Sande, C., 2019. Crop Monitoring Using Sentinel-1 Data: A Case Study from The Netherlands. Remote Sens. 2019 (11), 1887.

Klosterman, S.T., Hufkens, K., Gray, J.M., Melaas, E., Sonnentag, O., Lavine, I., Mitchell, L., Norman, R., Friedl, M.A., Richardson, A.D., 2014. Evaluating remote sensing of deciduous forest phenology at multiple spatial scales using PhenoCam imagery. Biogeosciences Discuss. 11 (16), 4305–4320.

Kowalski, K., Senf, C., Hostert, P., Pflugmacher, D., 2020. Characterizing spring phenology of temperate broadleaf forests using Landsat and Sentinel-2 time series. Int. J. Appl. Earth Obs. 92, 102172.

Lange, M., Dechant, B., Rebmann, C., Vohland, M., Cuntz, M., Doktor, D., 2017. Validating MODIS and Sentinel-2 NDVI Products at a Temperate Deciduous Forest Site Using Two Independent Ground-Based Sensors. Sensors 17, 1855.

Mandal, D., Hosseini, M., McNairn, H., Kumar, V., Bhattacharya, A., Rao, Y.S., Mitchell, S., Robertson, D.L., Davidson, A., Dabrowska-Zielinska, K., 2019. An investigation of inversion methodologies to retrieve the leaf area index of corn from C-band SAR data. Int. J. Appl. Earth Obs. 82 (2019), 101893.

Lucas, R.M., Moghaddam, M., Cronin, N., 2004. Microwave scattering from mixed-species forests, Queensland, Australia. IEEE Trans. Geosci. Remote Sens. 42 (10), 2142–2159.

Meerdink, S.K., Roberts, D.A., King, J.Y., Roth, K.L., Dennison, P.E., Amaral, C.H., Hook, S.J., 2016. Linking seasonal foliar traits to VSWIR-TIR spectroscopy across California ecosystems, Remote Sens. Environ. 186, 322–338.

Omar, H., Misman, M.A., Kassim, A.R., 2017. Synergetic of PALSAR-2 and Sentinel-1A SAR Polarimetry for Retrieving Aboveground Biomass in Dipterocarp Forest of Malaysia. Appl. Sci. 2017 (7), 675.

Ose, K., Corpetti, T., Demagistri, L., 2016. Multispectral Satellite Image Processing. In: Baghdadi, N., Zribi, M. (Eds.), Optical remote sensing of land surface techniques and methods. Elsevier, pp. 57–124.

Proietti, R., Antonucci, S., Monteverdi, M.C., Garfì, V., Marchetti, M., Plutino, M., Di Carlo, M., Germani, A., Santopuoli, G., Castaldi, C., Chiavetta, U., 2020. Monitoring spring phenology in Mediterranean beech populations through in situ observation and Synthetic Aperture Radar methods. Remote Sens. Environ. 248, 111978.

Proisy, C., Mougin, E., Dufrêne, E., Le Dantec, V., 2000. Monitoring seasonal changes of a mixed temperate forest using ERS SAR observations. IEEE T. Geosci. Remote Sens. 38, 540–552.

R Core Team, 2018. R: A language and environment for statistical computing. R Foundation for Statistical Computing, Vienna, Austria https://www.R-project.org/.

Reed, B.R., White, M.A., Brown, J.F., 2003. Remote sensing phenology. In: Schwartz, M. D. (Ed.), Phenology: An Integrative Environmental Science. Kluwer Academic Publishers, pp. 365–381.

Richardson, A.D., Black, T.A., Ciais, P., Delbart, N., Friedl, M.A., Gobron, N., Hollinger, D.Y., Kutsch, W.L., Longdoz, B., Luyssaert, S., Migliavacca, M., Montagnani, L., Munger, J.W., Moors, E., Piao, S., Rebmann, C., Reichstein, M., Saigusa, N., Tomelleri, E., Vargas, R., Varlagin, A., 2010. Influence of spring and autumn phenological transitions on forest ecosystem productivity. Philos. Trans. R. Soc. Lond., B Biol. Sci. 365, 3227–3246.

Richardson, A.D., Hufkens, K., Milliman, T., Aubrecht, D.M., Chen, M., Gray, J.M., Johnston, M.R., Keenan, T.F., Klosterman, S.T., Kosmala, M., Melaas, E.K., Friedl, M. A., Frolking, S., 2018. Tracking vegetation phenology across diverse North American biomes using PhenoCam imagery. Sci Data 5, 1–24.

Rüetschi, M., Schaepman, E.M., Small, D., 2018. Using Multitemporal Sentinel-1 C-band Backscatter to Monitor Phenology and Classify Deciduous and Coniferous Forests in Northern Switzerland. Remote Sens. 2018, 10.

Rüetschi, M., Small, D., Waser, L.T., 2019. Rapid Detection of Windthrows Using Sentinel-1 C-Band SAR Data. Remote Sens. 11, 115.

Schaber, J., Badeck, F.W., 2002. Evaluation of methods for the combination of phenological time series and outlier detection. Tree Physiol. 22, 973–982.

Song, Y., Wang, J., 2019. Mapping Winter Wheat Planting Area and Monitoring Its Phenology Using Sentinel-1 Backscatter Time Series. Remote Sens. 2019 (11), 449.

Schmidt, K., Tous Ramon, N., Schwerdt, M., 2018. Radiometric accuracy and stability of sentinel-1A determined using point targets. Int. J. Microw. Wirel. Technol. 10 (5–6), 538–546.

Soudani, K., Delpierre, N., Berveiller, D., Hmimina, G., Pontailler, J.-Y., Seureau, L., Vincent, G., Dufrêne, É., 2021. A survey of proximal methods for monitoring leaf phenology in temperate deciduous forests. Biogeosciences 18, 3391–3408.

Soudani, K., le Maire, G., Dufrêne, E., François, C., Delpierre, N., Ulrich, E., Cecchini, S., 2008. Evaluation of the onset of green-up in temperate deciduous broadleaf forests derived from Moderate Resolution Imaging Spectroradiometer (MODIS) data. Remote Sens. Environ. 12, 2643–2655.

Soudani, K., Hmimina, G., Delpierre, N., Pontailler, J.-Y., Aubinet, M., Bonal, D., Caquet, B., de Grandcourt, A., Burban, B., Flechard, C., Guyon, D., Granier, A., Gross, P., Heinesh, B., Longdoz, B., Loustau, D., Moureaux, C., Ourcival, J.-M., Rambal, S., Saint André, L., Dufrêne, E., 2012. Ground-based Network of NDVI measurements for tracking temporal dynamics of canopy structure and vegetation phenology in different biomes. Remote Sens. Environ. 123, 234–245.

Stendardi, L., Karlsen, S.R., Niedrist, G., Gerdol, R., Zebisch, M., Rossi, M., Notarnicola, C., 2019. Exploiting Time Series of Sentinel-1 and Sentinel-2 Imagery to Detect Meadow Phenology in Mountain Regions. Remote Sens. 2019 (11), 542.

Sudmanns, M., Tiede, D., Augustin, H., Lang, S., 2019. Assessing global Sentinel-2 coverage dynamics and data availability for operational Earth observation (EO) applications using the EO-Compass. Int. J. Digit. Earth 1–17.

Vavlas, N.-C., Waine, T.W., Meersmans, J., Burgess, P.J., Fontanelli, G., Richter, G.M., 2020. Deriving Wheat Crop Productivity Indicators Using Sentinel-1 Time Series. Remote Sens. 2020 (12), 2385.

Veloso, A., Mermoz, S., Bouvet, A., Le Toan, T., Planells, M., Dejoux, J.-F., Ceschia, E., 2017. Understanding the temporal behavior of crops using Sentinel-1 and Sentinel-2-like data for agricultural applications. Remote Sens. Environ. 199 (2017), 415–426.

Vreugdenhil, M., Wagner, W., Bauer-Marschallinger, B., Pfeil, I., Teubner, I., Rüdiger, C., Strauss, P., 2018. Sensitivity of Sentinel-1 Backscatter to Vegetation Dynamics: An Austrian Case Study. Remote Sens. 2018 (10), 1396.

Vrieling, A., Meroni, M., Darvishzadeh, R., Skidmore, A.K., Wang, T., Zurita-Milla, R., Oosterbeek, K., O'Connor, B., Paganini, M., 2018. Vegetation phenology from Sentinel-2 and field cameras for a Dutch barrier island. Remote Sens. Environ. 2018 (215), 517–529.

Yang, X., Tang, J., Mustard, J.F., Wu, J., Zhao, K., Serbin, S., Lee, J.E., 2016. Seasonal variability of multiple leaf traits captured by leaf spectroscopy at two temperate deciduous forests. Remote Sens. Environ. 179, 1–12.

Yang, H., Yang, X., Heskel, M., Sun, S., Tang, J., 2017. Seasonal variations of leaf and canopy properties tracked by ground-based NDVI imagery in a temperate forest. Sci. Rep. 7 (1), 1267.

Wang, J., Xiao, X., Bajgain, R., Starks, P., Steiner, J., Doughty, R.B., Chang, Q., 2019. Estimating leaf area index and aboveground biomass of grazing pastures using Sentinel-1, Sentinel-2 and Landsat images. ISPRS J. Photogramm. Remote Sens. 154, 189–201.

Wang, Q., Atkinson, P.M., 2018. Spatio-temporal fusion for daily Sentinel-2 images. Remote Sens. Environ. 204, 31–42.

White, J.C., Wulder, M.A., 2013. The Landsat observation record of Canada: 1972–2012. Can. J. Remote Sensing 39 (6), 455–467.

Woodhouse, I.H., 2001. The ratio of the arithmetic to the geometric mean: a cross-entropy interpretation. IEEE Trans. Geosci. Remote Sens. 39 (1), 188–189.

Zhang, X., Friedl, M.A., Schaaf, C.B., Strahler, A.H., Hodges, J.C.F., Gao, F., Reed, B.C., Huete, A., 2003. Monitoring vegetation phenology using MODIS. Remote Sens. Environ. 84, 471–475.